5-2022

Motility of *Escherichia coli* Near Surfaces

Mikayla M. Greiner
Trinity University, mgreiner@trinity.edu

Recommended Citation
Greiner, Mikayla M., "Motility of *Escherichia coli* Near Surfaces" (2022). *Physics & Astronomy Honors Theses*. 19.
https://digitalcommons.trinity.edu/physics_honors/19

(Motility of *Escherichia coli* Near Surfaces)

(Mikayla M. Greiner)

A departmental senior thesis submitted to the Department of Computer Science at Trinity University in partial fulfillment of the requirements for graduation with departmental honors.

(4/29/2022)

Thesis Advisor

Department Chair

Jennifer Henderson, AVPAA

Student Agreement

I grant Trinity University ("Institution"), my academic department ("Department"), and the Texas Digital Library ("TDL") the non-exclusive rights to copy, display, perform, distribute and publish the content I submit to this repository (hereafter called "Work") and to make the Work available in any format in perpetuity as part of a TDL, digital preservation program, Institution or Department repository communication or distribution effort.

I understand that once the Work is submitted, a bibliographic citation to the Work can remain visible in perpetuity, even if the Work is updated or removed.

I understand that the Work's copyright owner(s) will continue to own copyright outside these non-exclusive granted rights.

I warrant that:

1) I am the copyright owner of the Work, or
2) I am one of the copyright owners and have permission from the other owners to submit the Work, or
3) My Institution or Department is the copyright owner and I have permission to submit the Work, or
4) Another party is the copyright owner and I have permission to submit the Work.

Based on this, I further warrant to my knowledge:

1) The Work does not infringe any copyright, patent, or trade secrets of any third party,
2) The Work does not contain any libelous matter, nor invade the privacy of any person or third party, and
3) That no right in the Work has been sold, mortgaged, or otherwise disposed of, and is free from all claims.

I agree to hold TDL, DPN, Institution, Department, and their agents harmless for any liability arising from any breach of the above warranties or any claim of intellectual property infringement arising from the exercise of these non-exclusive granted rights."

I choose the following option for sharing my thesis (required):

[X] Open Access (full-text discoverable via search engines)
[ ] Restricted to campus viewing only (allow access only on the Trinity University campus via digitalcommons.trinity.edu)

I choose to append the following Creative Commons license (optional): CC BY-NC

Motility of *Escherichia coli* Near Surfaces

by

Mikayla M. Greiner

An honors thesis submitted to the Department of Physics & Astronomy at

TRINITY UNIVERSITY

in partial fulfillment of the requirements for the
Bachelor of Science in Applied Physics with Honors
May 2022

Accepted by ....
Prof. Kelvin Cheng

Accepted by ....
Prof. Nirav Mehta

Accepted by ....
Prof. David Pooley

Accepted by ....
Prof. Orrin Shindell

Accepted by ....
Prof. Jennifer Steele, Chair

Accepted by ....
Prof. Niescja Turner

Accepted by ....
Prof. Dennis Ugolini

Motility of *Escherichia coli* Near Surfaces

by

Mikayla M. Greiner

Submitted to the Department of Physics & Astronomy
on April 29, 2022, in partial fulfillment of the
requirements for the Bachelor of Science in Applied Physics with Honors

Abstract

Most bacteria, including the well-studied *Escherichia coli*, exist in two modes of life: individual cells swimming in bulk fluid, and cells that have aggregated on surfaces in relatively immotile communities. In bulk fluid, *E. coli* swims in relatively straight paths. However, as *E. coli* approaches a surface, hydrodynamic interactions between the bacterium and the surrounding fluid change, causing the bacterium to acquire circular trajectories. This near-surface swimming behavior provides a measure of what bacteria experience as they transition from free swimming to surface aggregation, which is an important step in early biofilm formation.

Here we examine the near-surface dynamics of *E. coli*. We present a new method for imaging and analyzing near-surface swimming dynamics involving TIRF microscopy and computational image analysis. TIRF microscopy is used to record *E. coli* swimming near a surface. The raw TIRF microscopy data is passed to custom MATLAB code that tracks the bacteria, reconstructs their trajectories in three dimensions, and extracts measurements of near-surface dynamics. We aim to validate our methodology by measuring cell motility near glass surfaces, which has been previously studied and quantified for *E. coli*. Once we validate our methodology, we plan to expand the scope of our experiment to study how properties of the surface affect near-surface motility. We present a plan to synthesize new biomimetic surfaces with tunable viscosity and outline methods to characterize the surfaces. These biomimetic surfaces will be used in future bacterial motility experiments to examine the relationship between near-surface dynamics and surface viscosity.

Thesis Supervisor: Prof. O. Shindell

Acknowledgements

I would like to thank the Department of Physics and Astronomy for their support over the past three years; the Trinity University Mach and Murchison Research Fellowships, which provided research funding; and my predecessors in the project, whose work forms the foundation of this thesis. This work is, in particular, a continuation of research conducted by Keaton Holt and Quân Hoàng.

Finally, I would like to thank my advisor, Professor Orrin Shindell, whose mentorship and infectious love of biophysics made this work possible. Thank you for your unfailing support and guidance.

Contents

Chapter 1

Background

1.1 Introduction

Most bacteria exist in two modes of life: individual free-swimming cells, and surface-aggregated communities called biofilms. The transition between the two is marked by unique motility near surfaces. As bacteria approach a surface, they experience hydrodynamic forces that confine their motion to translocation along the surface boundary [1, 2, 3, 4]. This near-surface confinement is often accompanied by other changes in motility, as is the case with the well-studied bacterium *Escherichia coli.* In bulk fluid, *E. coli* swims in relatively straight paths. However, as *E. coli* approaches a solid surface, hydrodynamic cell-surface interactions cause the bacterium to acquire circular trajectories. Previous experimental work has measured the dynamics of bacteria swimming above a glass coverslip, making it possible to begin studying the kinds of cell-surface interactions that bacteria experience during near-surface swimming [1, 5, 3, 6, 7]. However, a glass coverslip is quite different from the complex biological surfaces that bacteria encounter when colonizing a host organism. Our goal is to study how certain characteristics of these complex surfaces, such as viscosity and charge, affect near-surface motility.

In this thesis, we examine bacterial near-surface swimming using *E. coli* as a model organism. We present a method to extract three-dimensional near-surface dynamics using microscopy and computational analysis. In particular, we recorded the near-surface motility of fluorescent *E. coli* using TIRF microscopy. We then developed custom MATLAB code to extract motility measurements from TIRF microscopy data. We first measured motility above a glass coverslip. Measurements of interest include cell speed, curvature of the trajectory, and cell orientation relative to the surface normal. Measurements of cell orientation have largely been restricted to theoretical predictions; thus, we expect our research to contribute to wider experimental measurements of *E. coli* dynamics. On the other hand, cell speed and trajectory curvature have previously been measured as a function of height above the surface. Our aim is to reach a quantitative match with published speed and curvature values in order to validate our methodology. We can then proceed to use our methods to measure bacterial motility above more complex surfaces. In particular, we plan to construct biomimetic surfaces for our experiments. The purpose of using these surfaces is twofold: first, to introduce greater biological realism into the experiments; and second, to determine the effect of specific surface properties on near-surface motility. We present our current progress in synthesizing biomimetic surfaces of tunable viscosity for use in bacterial motility experiments. Finally, we comment on future directions of the project.

1.2 Background: Bacterial Motility

Most bacteria are motile, exploring the world around them through a variety of motility mechanisms in order to search for food, evade predators, and find places to replicate and grow. A common method of motility is propulsion using a flagellum or multiple flagella. E. coli, like many other bacteria, is a peritrichous bacterium; it is propelled by multiple helical flagella anchored at various points along the cell body. These flagella are driven by a protein motor that can rotate clockwise or counterclockwise. When *E. coli* rotates its flagella counterclockwise, as viewed from behind the bacterium, the flagella form a helical bundle that drives *E. coli* forward. When *E. coli* rotates its flagella clockwise, they unbundle and cause E. coli to experience a random change in direction. The result is a "run and tumble" motility mechanism, wherein *E. coli* swims in relatively straight lines (runs) interrupted by random reorientations (tumbles) [8].

E. coli can actively alter its motility in response to a variety of environmental conditions, including pH, chemical concentrations, and temperature. For instance, *E. coli* is a chemotactic bacterium, meaning that it can sense changes in chemical concentration and respond by swimming up or down the chemical gradient. In this case, *E. coli* changes its swimming direction by controlling the frequency of runs and tumbles. If the bacterium senses that it is moving in a favorable direction, it exhibits fewer tumbles, allowing it to continue moving forward. If the bacterium is moving in an unfavorable direction, it exhibits more frequent tumbles, increasing the chance that it will be reoriented in a different direction.

However, physical constraints of the environment itself can also influence bacterial motility patterns. An example of particular interest to our research occurs when *E. coli* swims near a solid-liquid interface. When *E. coli* undergoes runs in bulk fluid, it swims in smooth, relatively straight paths. However, when *E. coli* approaches a solid surface, it adopts roughly circular trajectories in the clockwise direction, as viewed from above. Current research suggests that these circular trajectories arise as a consequence of hydrodynamic interactions between the cell and the surface [1] (see Section 1.3). Furthermore, cells often become trapped in these near-surface trajectories; that is, the cell continues to swim in circles parallel and at close proximity to the surface until an event, such as a tumble or a transient cell-surface adhesion event, causes the cell to depart from the wall [9, 10]. Previous work suggests that when certain strains of *E. coli* engage in near-surface swimming, the frequency of transient surface adhesion events matches the value predicted to maximize surface exploration [9].

Because bacteria spend a significant portion of their life cycle living near surfaces, there are a number of reasons why bacteria may spend time exploring surfaces or interfaces between mediums. In an aquatic environment, nutrients may accumulate in sediment lining the bottom of a body of water, or become concentrated near the air-water interface. On the other hand, for bacteria that live inside of hosts, near-surface exploration may play a role in guiding cells towards places where they can anchor themselves and form surface aggregates; or, in the case of pathogenic bacteria, sites where the bacteria can invade and attack host tissue [11]. In both cases, quantifying near-surface dynamics provides insight into what bacteria experience as they navigate such interfaces. Understanding such behavior has important applications in the medical field, as biofilm formation on medical implants or chronic wounds can give rise to serious infections [12, 13]. More broadly, near-surface swimming dynamics can also provide insight into the evolutionary relationship between bacterial surface exploration and morphology. It stands to reason that bacteria acquire particular structural geometries because they maximize survival. For instance, flagella of a particular length or cell bodies of a particular size may be more efficient than others, allowing cells to minimize the energy they expend exploring surfaces.

1.3 Hydrodynamic Influences on Near-Surface Swimming Behavior

Here we describe the physical constraints that give rise to the characteristic features of near-surface swimming. Previously published work suggests that hydrodynamic interactions between swimming bacteria and solid surfaces can account for the near-surface motility patterns exhibited by *E. coli* and bacteria of a similar morphology [1, 5, 10]. As *E. coli* swims, it rotates its flagellar bundle counterclockwise, and its body counter-rotates clockwise, as viewed from behind the bacterium. The flagellar bundle exerts a force on the surrounding fluid that propels the bacterium forward. In turn, the surrounding fluid exerts a drag force on the bacterium. For low Reynolds number conditions, as is the case here, the net force and net torque on the bacterium must be zero. Therefore, the fluid drag force and propulsive force balance so that, for a given rotation rate, the bacterium moves at a constant velocity. Net torque must also be zero, so the rotation rate of the bacterium around its own swimming axis is constant, explained by a balance of the torque associated with cell rotation with viscous drag. In bulk fluid, the result is that *E. coli* swims straight forward with constant velocity.

As the cell approaches a surface, the drag forces acting on the bacterium change. Specifically, the fluid drag force increases with greater proximity to the surface. Parts of the cell that are closer to the surface will therefore experience stronger drag forces than parts of the cell that are farther from the surface. As a result, the clockwise-rotating body and counterclockwise-rotating flagellar bundle both experience a net force in opposite lateral directions. Low Reynolds number conditions still apply, so these forces will balance out to give zero net force. However, these forces introduce a torque on the entire cell that causes the cell to move in clockwise circular trajectories, as viewed from above. The torque is balanced by viscous drag such that the cell traces out the circular trajectory at a constant angular velocity. Figure 1-1 summarizes these hydrodynamic interactions.

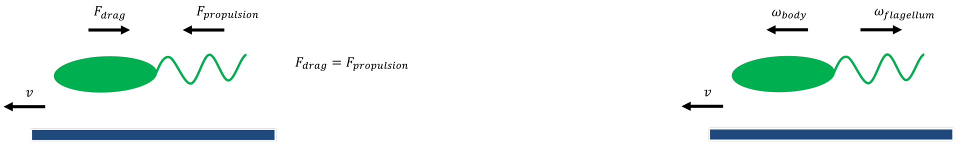

(a) The flagellar bundle generates a propulsive force, driving the bacterium forward. Fluid drag opposes the propulsive force. At a low Reynolds number, these forces cancel, and the bacterium swims at constant velocity.

(b) As the flagellar bundle rotates at angular speed $\omega_{flagellum}$, the cell body counter-rotates at angular speed ω_{body}. The angular velocity vectors shown above indicate the direction of rotation by the right-hand-rule.

(c) Fluid drag forces oppose the rotation of the cell body and flagellum. The fluid drag forces are represented by the circles on the cell body and flagellum; circles containing a dot indicate a drag force directed out of the page, while circles containing an x indicate a drag force directed into the page. The size of the circle suggests the relative magnitude of the force. Note that the drag forces acting on the bacterium are larger near the surface.

(d) Strong drag forces on the bottom of the bacterium in figure (c) give rise to equal and opposite net forces on the body and the flagellum. Although these forces cancel to give zero net force, they introduce a torque on the bacterium. This causes the bacterium to move in a circular path. Since we expect the bacterium to be torque-free, the bacterium moves at a constant angular velocity $\omega_{bacterium}$. The angular velocity vector indicates the direction of circular motion, given by the right-hand rule.

Figure 1-1: A summary of how hydrodynamic interactions give rise to characteristic features of near-surface swimming. Ultimately, the bacterium is torque-free and force-free, swims at a constant speed, and traces out clockwise circular trajectories, as viewed from above.

Chapter 2

TIRF Microscopy

2.1 Introduction

The microscopy technique we use to observe near-surface swimming is Total Internal Reflection Fluorescence (TIRF) Microscopy. This technique relies on optical phenomena that occur when light encounters a boundary between two optical media. With TIRF microscopy, fluorescent samples can be imaged with high axial resolution and low background noise. The high axial resolution that TIRF offers is critical to our study of near-surface motility, since being able to distinguish the position of fluorescent cells relative to the surface is an important factor in our analysis. In this chapter, we include theoretical considerations relevant to TIRF microscopy and describe preliminary experiments in which use TIRF microscopy to record near-surface swimming.

2.2 Total Internal Reflection

When light is incident on a boundary between two mediums with different indices of refraction n_1 and n_2, the light may be partially reflected and transmitted. Figure 2-1a illustrates the geometry of the situation. The incident, transmitted, and reflected rays are coplanar, and are oriented at angles θ_1, θ_2, and θ_3 relative to the surface normal. The law of reflection states that

$$\theta_1 = \theta_3 \tag{2.1}$$

which means that the incident and reflected rays are oriented at the same angle with respect to the normal. On the other hand, the transmitted light will be refracted, such that the angle it makes with the surface normal differs from the angle of incidence. The relationship between the incident and transmitted angles is given by Snell's law,

$$n_1 \sin(\theta_1) = n_2 \sin(\theta_2) \tag{2.2}$$

where θ_1 is the angle of incidence and θ_2 is the angle of refraction.

Notice that if $n_1 > n_2$, then we must have $\theta_1 < \theta_2$, since both angles are constrained between 0 and 90 degrees. In other words, if the index of refraction of the incident medium (n_1) is greater than that of

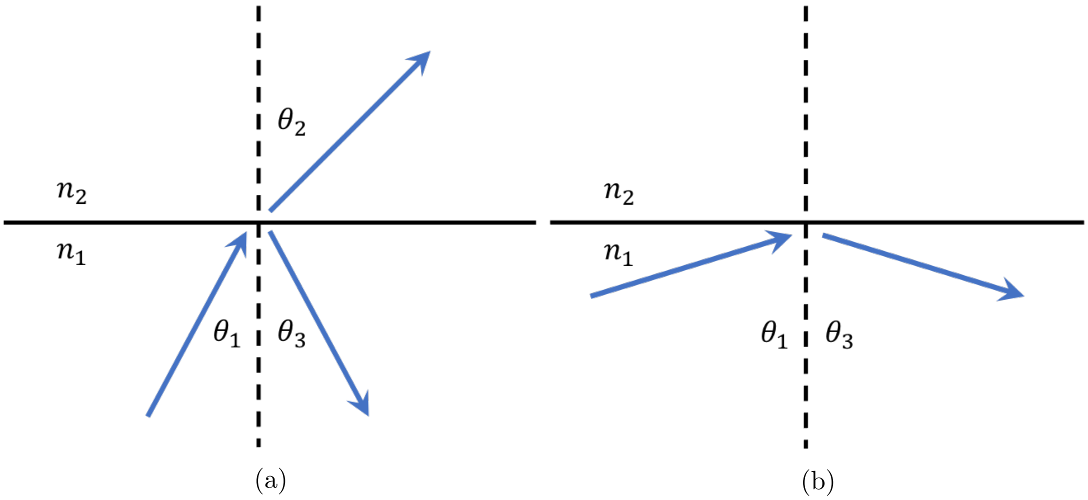

Figure 2-1: (a) Light incident on a boundary between optical media with different indices of refraction may partially reflect and transmit. (b) Total internal reflection.

the transmitting medium (n_2), then light is refracted at an angle greater than the incident angle. In these circumstances, it is possible to increase θ_1 to the point where θ_2 reaches 90°. The value of θ_1 at which this occurs is called the critical angle. In terms of Snell's law (Equation 2.2), we see that

$$n_1 \sin(\theta_c) = n_2 \sin(90°) \Rightarrow \tag{2.3}$$

$$\sin(\theta_c) = \frac{n_2}{n_1} \tag{2.4}$$

where θ_c is the critical angle. Beyond the critical angle, light no longer transmits past the boundary and is only reflected. This phenomenon is referred to as total internal reflection (Figure 2-1b).

A notable feature of total internal reflection is that electromagnetic radiation is present on both sides of the surface. Although the transmitted ray in Figure 2-1 no longer appears, an electromagnetic field still forms on the other side of the boundary. This field is referred to as the evanescent wave. It is possible to derive the existence of the evanescent wave by reexamining the situation in Figure 2-1 for an incident plane wave. For an incident plane wave, the electric fields associated with the incident, transmitted, and reflected rays take the form of

$$\vec{E_i} = \vec{E_1} e^{i\left(\vec{k_1}\cdot\vec{r}-\omega t\right)} \tag{2.5}$$

$$\vec{E_t} = \vec{E_2} e^{i\left(\vec{k_2}\cdot\vec{r}-\omega t\right)} \tag{2.6}$$

$$\vec{E_r} = \vec{E_3} e^{i\left(\vec{k_3}\cdot\vec{r}-\omega t\right)} \tag{2.7}$$

where the electric fields for the incident, transmitted, and reflected rays are $\vec{E_i}$, $\vec{E_t}$, and $\vec{E_r}$, respectively. Here, $\vec{r}$ is a position vector; ω is the angular frequency of the waves; $\vec{k_1}$, $\vec{k_2}$, and $\vec{k_3}$ are wave vectors; and $\vec{E_1}$, $\vec{E_2}$, and $\vec{E_3}$ are vector amplitudes. Without loss of generality, one can set up a coordinate system where $\vec{k_1}$, $\vec{k_2}$, and $\vec{k_3}$ lie in the yz-plane, and the boundary lies in the xy-plane (Figure 2-2).

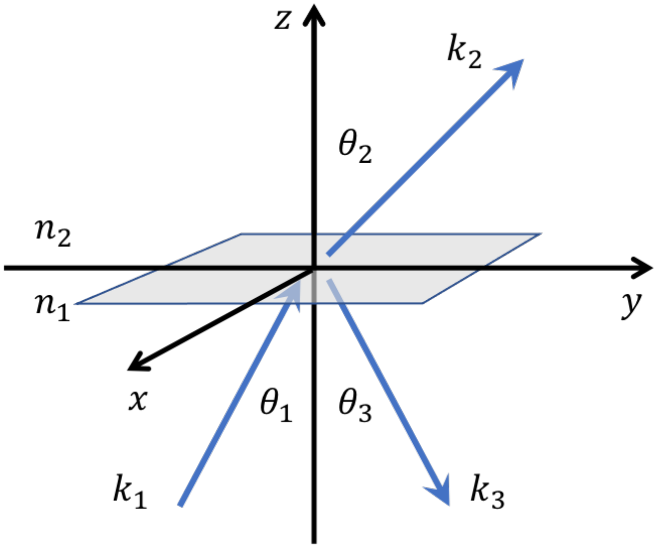

Figure 2-2: Incident, reflected, and transmitted rays.

Let us examine the transmitted field, $\vec{E_t}$. The wave vector $\vec{k_2}$ can be expressed as

$$\vec{k_2} = k_2 \sin(\theta_2)\hat{j} + k_2 \cos(\theta_2)\hat{k} \tag{2.8}$$

where $\hat{j}$ and $\hat{k}$ represent unit vectors in the y and z directions, respectively. If we take the position vector $\vec{r}$ to be

$$\vec{r} = x\hat{i} + y\hat{j} + z\hat{k} \tag{2.9}$$

then the dot product in the exponential of E'' can be written as

$$\vec{k_2} \cdot \vec{r} = k_2 y \sin(\theta_2) + k_2 z \cos(\theta_2) \tag{2.10}$$

In order to determine the effect of the incident angle θ_1 on the form of the transmitted wave E_t, we can rewrite $\sin\theta_2$ in terms of $\sin\theta_1$ using Snell's Law (Equation 2.2):

$$n_1 \sin(\theta_1) = n_2 \sin(\theta_2) \Rightarrow \tag{2.11}$$

$$\sin(\theta_2) = \frac{n_1}{n_2} \sin(\theta_1) \tag{2.12}$$

With some additional mathematical manipulation, we can also rewrite $\cos(\theta_2)$ in terms of $\sin(\theta_1)$:

$$\sin(\theta_2) = \frac{n_1}{n_2} \sin(\theta_1) \Rightarrow \tag{2.13}$$

$$\sin^2(\theta_2) = \left(\frac{n_1}{n_2}\right)^2 \sin^2(\theta_1) \Rightarrow \tag{2.14}$$

$$1-\cos^2(\theta_2)=\left(\frac{n_1}{n_2}\right)^2\sin^2(\theta_1)\Rightarrow \tag{2.15}$$

$$\cos(\theta_2)=\sqrt{1-\left(\frac{n_1}{n_2}\right)^2\sin^2(\theta_1)} \tag{2.16}$$

In the case of total internal reflection, we have

$$\sin(\theta_1)=\sin(\theta_c)=\frac{n_1}{n_2} \tag{2.17}$$

such that

$$\cos(\theta_2)=\sqrt{1-1}=0 \tag{2.18}$$

However, if θ_1 exceeds the critical angle, then

$$\sin(\theta_1)>\frac{n_1}{n_2} \tag{2.19}$$

which would make the argument under the radical in equation 2.16 negative. Consequently, we write

$$\cos(\theta_2)=i\sqrt{\left(\frac{n_1}{n_2}\right)^2\sin^2(\theta_1)-1} \tag{2.20}$$

where $\cos(\theta_2)$ is now imaginary. Returning to Equation 2.10, we see from Equations 2.12 and 2.20 that the dot product of the wave vector and the position vector becomes

$$\vec{k_2}\cdot\vec{r}=k_2y\left(\frac{n_1}{n_2}\right)\sin(\theta_1)+ik_2z\sqrt{\left(\frac{n_1}{n_2}\right)^2\sin^2(\theta_1)-1} \tag{2.21}$$

which, for simplicity, we may write as

$$\vec{k_2}\cdot\vec{r}=k'y+iz\alpha \tag{2.22}$$

where

$$\alpha\equiv k_2\sqrt{\left(\frac{n_1}{n_2}\right)^2\sin^2(\theta_1)-1} \tag{2.23}$$

$$k'\equiv k_2\left(\frac{n_1}{n_2}\right)\sin(\theta_1) \tag{2.24}$$

Finally, returning to the transmitted electric field vector in Equation 2.6, we find that

$$\vec{E_t}=\vec{E_2}e^{i(k'y+iz\alpha-\omega t)} \tag{2.25}$$

$$\vec{E_t}=\vec{E_2}e^{-\alpha z}e^{i(k'y-\omega t)} \tag{2.26}$$

where $z > 0$ for the region above the xy-plane of the surface. The first exponential term suggests that the waves decay exponentially with height by a constant α, which depends on the incident angle θ_1 and the ratio of the indices of refraction. The second exponential term suggests that the electromagnetic field consists of plane waves oriented parallel to the boundary. Eq. 2.26 is called the evanescent field. The intensity of this field can now be written as

$$I = I_0 e^{-z/d} \tag{2.27}$$

where I_0 is the maximum intensity, z is the height above the surface, and $d = 1/(2\alpha)$ is the penetration depth.

2.3 TIRF Microscopy

TIRF Microscopy takes advantage of the principle of total internal reflection and the evanescent wave to illuminate thin regions of a sample with high axial resolution. Although a few different methods exist for generating this evanescent wave, most modern TIRF systems use an objective-based method; this is the method employed in our experiments. First, the sample of interest - usually a solution containing fluorophores that can be excited by the incident light frequency - is dispensed onto a microscope coverslip. The index of refraction of the coverslip must be larger than that of the solution, which is typically the case for aqueous solutions. The coverslip holding the sample is then positioned above an oil objective. The index of refraction of the oil is carefully tuned to match that of the coverslip so that no refraction occurs at the oil-coverslip interface.

To illuminate the sample, a laser is directed up through the microscope objective. The laser beam transmits past the oil-glass interface with no refraction, since the two mediums have the same index of refraction. The beam then passes through the glass and is incident on the interface between the glass and the liquid sample. The laser is angled in such a way that when it encounters the glass-liquid interface, it totally internally reflects inside the glass. This generates an evanescent field on the liquid side of the interface. By Eq. 2.27, the intensity of the evanescent field diminishes exponentially with height above the coverslip. Therefore, the evanescent field only excites fluorophores within a thin region of the sample, typically between 75-750 nm above the surface.

This method of imaging is beneficial for a few reasons. First, background noise is significantly diminished [14]. As objects move higher up in the fluid, out of the plane of focus, they quickly fall outside of the region of fluorescent excitation. This also means that most of the signal comes from particles near the coverslip, within the plane of focus. In the context of our experiment, TIRF enables us to image near-surface swimming with less background noise from bacteria swimming further up away from the boundary. Second, because the evanescent field intensity decays rapidly with height above the surface, TIRF images have high axial resolution. This high axial resolution is integral to our analysis of near-surface motility, because it allows us to distinguish height differences along the length of a 1-2 µm-long bacterium (Figure 2-3). We can then extract important information about the bacterium's motion, including the bacterium's height above the surface and how the bacterium is tilted relative to the surface normal.

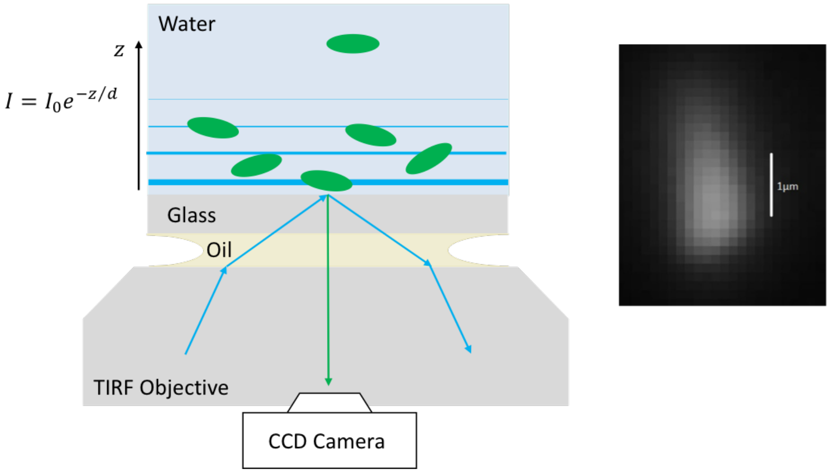

Figure 2-3: We use objective-based TIRF microscopy to observe fluorescent *E. coli* (green ellipses) swimming near a glass coverslip with high axial resolution. An example of our raw data is shown on the right. The brighter portion of the bacterium is tilted closer to the surface, while the dimmer portion is tilted away from the surface.

Further details regarding how we collect and analyze TIRF microscopy data can be found in the following chapter, in which we discuss our experimental methodology and computational analysis.

Chapter 3

Bacterial Motility

3.1 Introduction

In this section, we discuss our experimental methodology. We then describe the process by which we analyze experimental data using custom MATLAB code. Ultimately, this code allows us to extract measurements of near-surface dynamics, including cell speed, curvature of the trajectory, cell orientation, and cell height above the surface. A preliminary version of this code is available for discussion upon request, as the code is currently being withheld pending publication.

3.2 Experiments: Recording Near-Surface Swimming

TIRF microscopy was used to observe *E. coli* engaged in near-surface swimming above a glass coverslip. The *E. coli* used in our experiments were "smooth-swimming" CheY mutants. This strain is unable to tumble, so it swims in a continuous run. Consequently, near-surface trajectories are uninterrupted by tumbling events, which ensures that trajectories are long enough to provide sufficient data for analysis. Cells were also made to express GFP such that the cell body was fluorescent. Flagella were not made to fluoresce.

Free-swimming *E. coli* cells were suspended in motility medium. A sample of the *E. coli* suspension was pipetted onto a glass coverslip placed above a 100X oil objective. TIRF microscopy was then used to record videos of individual *E. coli* swimming in the fluid (Figure 3-1).

3.3 Overview of Computational Analysis

After experimental data is collected, the data undergoes computational processing. First, raw TIRF microscopy data is converted to a series of TIFF stacks in ImageJ. The TIFF stacks are then passed through custom MATLAB code in order to extract measurements of near-surface dynamics. Measurements of interest include the orientation of the bacterium relative to the surface normal while engaged in near-surface swimming, as well as cell speed and curvature of the trajectory as a function of height above the surface.

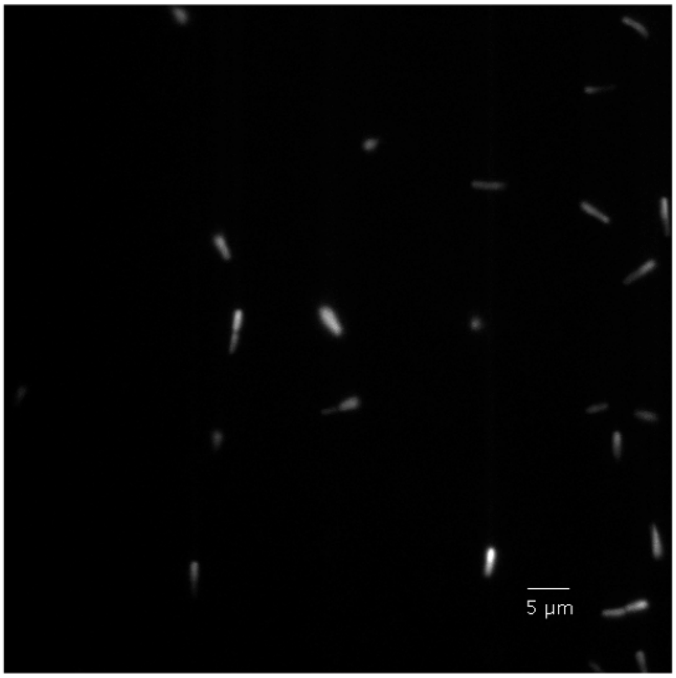

Figure 3-1: TIRF Microscopy data depicting smooth-swimming *Escherichia coli* swimming above a glass coverslip. Brighter bacteria are swimming at a lower height, closer to the glass coverslip; dimmer bacteria are swimming higher up in the fluid.

The custom MATLAB code analyzes the data in three main stages. First, it tracks the bacteria and isolates trajectories that are sufficiently long enough for analysis. Trajectories involving replicating bacteria and collisions between bacteria are filtered out of the data. Second, the code takes the remaining trajectories and reconstructs the motion of each bacterium in three dimensions. In these three-dimensional reconstructions, each bacterium is modeled as an ellipsoid. An ellipsoid-fitting algorithm is used to determine the appropriate dimensions of the ellipsoidal model for each particular bacterium. Once the appropriate dimensions are chosen, the fitting algorithm determines the bacterium's height above the surface and the vertical tilt of the bacterium, which is characterized as the angle between the surface normal and the vector defining the major axis of the rod-shaped cell body. Once complete, the modeling process provides more accurate information about the bacterium's position and orientation in three-dimensional space. Third, using the new position and orientation information, the code extracts measurements of cell speed and curvature of the trajectory as a function of height above the surface. Cell orientation during near-surface swimming is plotted as a histogram to determine the most common orientation of the bacterium while engaged in near-surface swimming.

Greater detail about each stage of the computational analysis is included in the sections below.

3.4 Preparing Data for Analysis

First, the raw image data is rescaled for analysis. In practice, the evanescent field does not illuminate all regions of the sample in a perfectly uniform fashion, so some parts of an image will appear dimmer than others. It is necessary to account for these variations in illumination if we want to be able to relate the brightness of an object to its height above the surface, regardless of where that object is in the frame. Each frame of the raw image data is processed as follows. First, the image is broken up into small square-shaped regions. Typically, regions are 64 by 64 pixels in size (400 by 400 µm) for a frame size of 512 by 512 pixels (3200 by 3200 µm). We assume that every region is statistically identical because there is no reason for bacteria to prefer one region over the other.

The code then proceeds to rescale each region separately. First, the code finds the Gaussian distribution of the pixel intensities. For the *E. coli* concentrations we use, the number of background pixels is so much greater than the number of signal pixels that the distribution is approximately centered on the background distribution. The upper threshold for background intensities is selected to be four standard deviations above the mean. All pixels below the threshold value are assumed to be background, and are set to an intensity value of zero. We take the geometric mean of the intensities of the remaining pixels, which are assumed to be signal, and divide each pixel intensity by the geometric mean. The resulting image is properly scaled across each region, and can be passed on to the next portion of the code for further analysis.

3.5 Tracking Bacteria

Next, the code tracks the swimming bacteria and records their trajectories. The process begins with locating the bacteria. As the code goes through each frame of the video data, it finds objects whose area lays within a reasonable size range for *E. coli*, and assumes that to be an *E. coli* cell. It then records the location of the cell's brightest pixel. The data is passed through a series of filters to remove cases that could complicate results, such as cells that are colliding with other cells or sticking partially out of the frame. To exclude collisions between bacteria from analysis, the code throws out any points that are closer than 8 µm to another point in the same frame. Similarly, the code filters out bacteria that may pass out of the field of view by removing points closer than two body lengths (4 µm) from the edge of the frame. We also ignore replicating bacteria, which are longer than non-replicating bacteria and may exhibit different swimming dynamics. To filter out replicating bacteria, objects longer than a typical *E. coli* cell are removed from analysis.

We then determine the trajectories of the remaining bacteria. The code goes through the video frames sequentially and stitches together bacterial trajectories by finding points in close proximity to each other over successive frames. For instance, if points in frame 1 and frame 2 are closer than a certain distance, the points are considered to belong to the same bacterium. The points are then added to a list of coordinates describing that bacterium's trajectory. To ensure that the trajectories are long enough for analysis, trajectories with fewer than 30 coordinates are discarded.

The code now has a series of coordinates specifying each bacterium's position at each point in its trajectory (Figure 3-2). Equipped with these coordinates, the code returns to the scaled image data and extracts a close-up image of the bacteria at each point in their trajectories. The intensity profiles associated with these close-up images will be useful for the next portion of the analysis, which involves making three-dimensional models of the bacteria to reconstruct their motion in three-dimensional space.

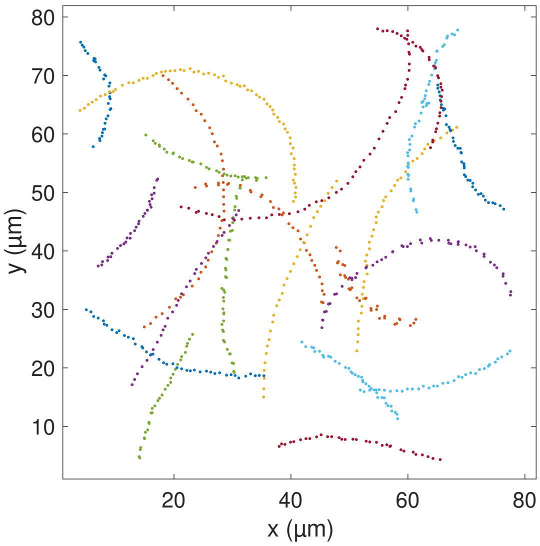

Figure 3-2: Circular trajectories of smooth-swimming *E. coli* swimming near a glass coverslip. Each set of colored dots corresponds to a different trajectory. Note that not all trajectories correspond to the same time points; bacteria that appear to cross paths simply traversed the same location at different times.

3.6 Reconstructing Trajectories in Three Dimensions: Ellipsoid-Fitting Algorithm

Up until this point, we have been working with two-dimensional image data. However, because near-surface swimming is inherently tied to a bacterium's proximity to the surface, it is important to understand how motion parallel to the surface plane depends quantitatively on height. This section describes our methodology for extracting three-dimensional position and orientation information from two-dimensional image data.

We characterize the bacterium's three-dimensional position and orientation using five quantities: the bacterium's x, y, and z coordinates, and the angles ϕ and θ, which define the bacterium's orientation within the surface plane and relative to the surface normal, respectively (Figure 3-3). To determine these values, we model the rod-shaped *E. coli* cell body as an ellipsoid in three-dimensional space. Our ellipsoid-fitting algorithm goes through a series of steps to fit an ellipsoid of proper dimensions and orientation to the bacterium at each point in its trajectory. In essence, we generate a large set of ellipsoids with different dimensions, create hypothetical image data for each ellipsoid, and compare the hypothetical image data to the real image data. The proper ellipsoidal model is then selected using a least-squares method.

To generate hypothetical image data, we use the relationship between fluorescent intensity and height given by Equation 2.27. When fluorophores are observed using TIRF microscopy, the measured intensity of the fluorophore diminishes exponentially with height above the surface. This characteristic decay in fluorescent intensity provides a means by which we can extract information about a bacterium's position above the surface, given its intensity profile; or in this case, predict the intensity profile of a model bacterium, given its position above the surface. To predict the intensity profile, we calculate the hypothetical intensity at each point along the ellipsoidal model as a function of height above the surface and penetration

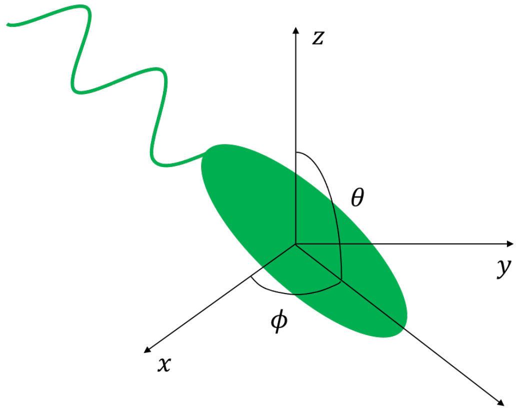

Figure 3-3: Five coordinates of interest define the bacterium's position and orientation: the x, y, and z coordinates of the bacterium's center; ϕ, the angle between the x-axis and the projection of the vector through the cell body's major axis onto the xy-plane; and θ, the angle between the z-axis and the vector through the cell body's major axis.

depth of the microscope.

However, before we compare the hypothetical intensity data to real intensity data, we must account for one other experimental factor: the diffraction of light as it propagates through the microscope. This diffraction causes each fluorescent point particle to be detected as a spread of intensity. We can mimic this effect using a point spread function. To calibrate the point spread function for our particular setup, we use TIRF microscopy to image a fluorescent polystyrene sphere of known diameter and fit an Airy disk to the resulting data. We then convolute the hypothetical intensity data with the Airy disk. The result is a hypothetical image of the ellipsoidal model, which can now be directly compared to real image data of a bacterium.

3.6.1 Fitting Procedure

First, the code calculates the angle ϕ at which the bacterium is rotated relative to the x-axis. The code takes the intensity profile of the bacterium, which may initially be oriented at any angle ϕ in the surface plane, and sets up a moment of inertia matrix for the cell. The data is rotated so that the major axis of the cell lies along the x-axis. This process is repeated for every intensity profile in the bacterium's trajectory.

Next, the ellipsoid-fitting algorithm determines the dimensions of the ellipsoidal model. Because different bacteria may vary slightly in size, it is necessary to determine the dimensions of each bacterium individually. To determine the semimajor and semiminor axis lengths of the bacterium, the code finds the frame in which the bacterium is oriented most parallel to the surface, which is taken to be the intensity profile with the longest major axis. The code generates a series of ellipsoids with varying semiminor and semimajor axes, all parallel to the xy-plane, and uses a least-squares method to fit an ellipsoid to the selected profile.

Once the code has calculated the dimensions of the bacterium, it moves on to determining the xz-orientation (θ) of the bacterium at each timestep. The code takes the ellipsoid from the previous step, and evaluates the fit for varying values of θ, ranging from 0 to $\frac{\pi}{2}$. Again, a least-squares method is used to select the best-fitting ellipsoid. The process is repeated for each timestep in the trajectory.

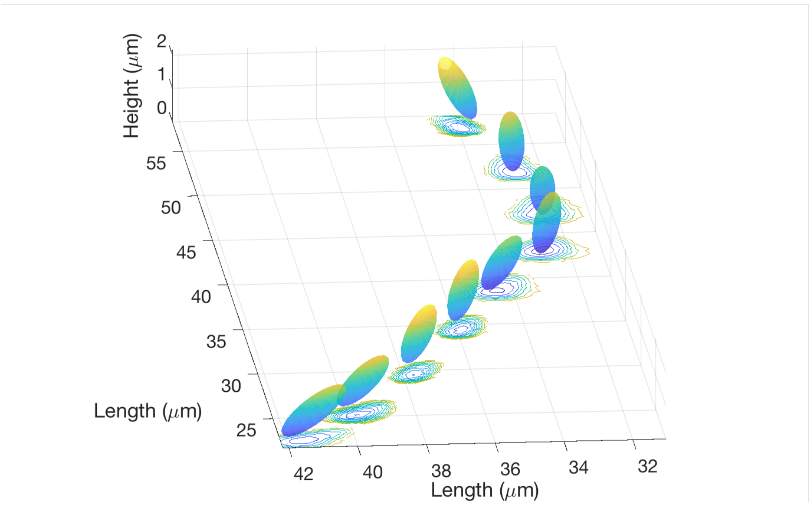

Figure 3-4: Trajectory of an *E. coli* cell observed using TIRF microscopy, reconstructed in three dimensions.

Finally, the lowest z-position of the bacterium is determined by applying Equation 2.27 to the brightest pixel in the bacterium's intensity profile. This z-coordinate is used to properly position the ellipsoidal model. Once the modeling procedure is complete, the bacterium's trajectory can be reconstructed in three-dimensional space (Figure 3-4).

3.7 Extracting Measurements

Once the trajectory has been reconstructed, we proceed to extract measurements of near-surface dynamics. We begin by returning to the trajectories shown in Figure 3-2. Initially, each point in the trajectory was defined as the (x, y) coordinate of the brightest pixel on the bacterium. We now redefine these points with the (x, y, z) coordinate of the center of the bacterium, as indicated by the ellipsoidal model. Using these coordinates, we can measure the bacterium's speed, the curvature of the trajectory, and the bacterium's height above the surface. Note that although the trajectories shown in Figure 3-2 are roughly circular, the curvature can vary along the course of a single trajectory. To account for these variations in curvature, we split each trajectory into segments, each containing about 15 points, and analyze each segment separately (Figure 3-5a). A circle is fit to each segment (Figure 3-5b). The bacterium's average speed v over that segment is defined as

$$v = \frac{S}{\Delta t} \tag{3.1}$$

where S is the arclength of the fitted circle between the initial and final points and Δt is the time elapsed. The curvature κ of the trajectory is defined as

$$\kappa = \frac{1}{R} \tag{3.2}$$

where R is the radius of the fitted circle. The bacterium's average height above the surface can also be calculated by averaging the z-coordinates of each point in the segment. It is then possible to plot average speed and curvature as a function of height. See Section 3.8 for preliminary results.

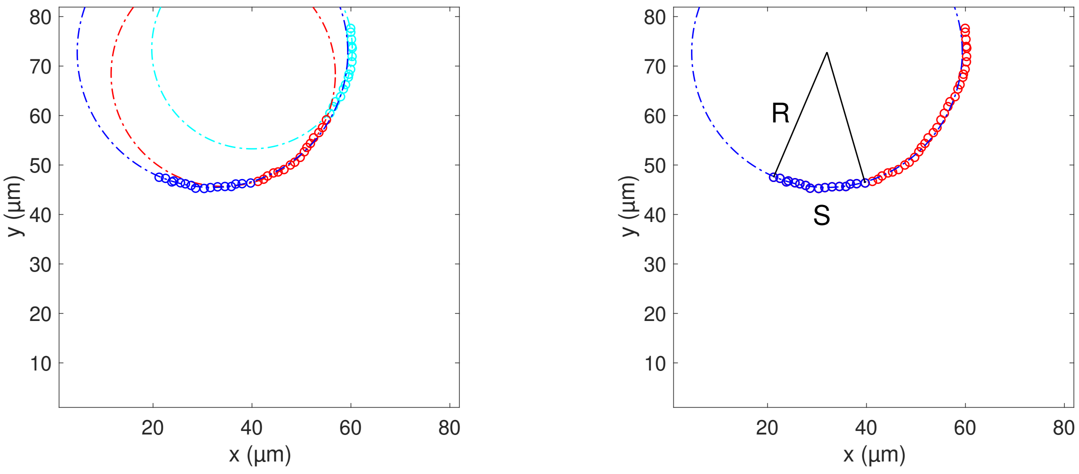

(a) (b)

Figure 3-5: (a) A trajectory has been split into three parts - the points labeled in blue, red, and light blue - which will be analyzed separately. (b) Analyzing near-surface dynamics over an individual part of the trajectory (blue). We fit a circle to the section of interest, then use the circle to calculate speed and curvature.

3.8 Results: Preliminary Measurements

Here we present preliminary results for smooth-swimming *E. coli* swimming above a glass coverslip. the average speed of the bacterium and curvature of the trajectory are plotted as a function of height above the surface (Figure 3-6). Based on previously published work, we expected that as height increased, speed would increase and curvature would decrease [3, 5, 6, 7]. Although these trends are roughly visible in the figures shown, there is considerable scatter in both plots. One factor that may be affecting these results is that the data has not been sorted to account for differences in cell orientation and size.

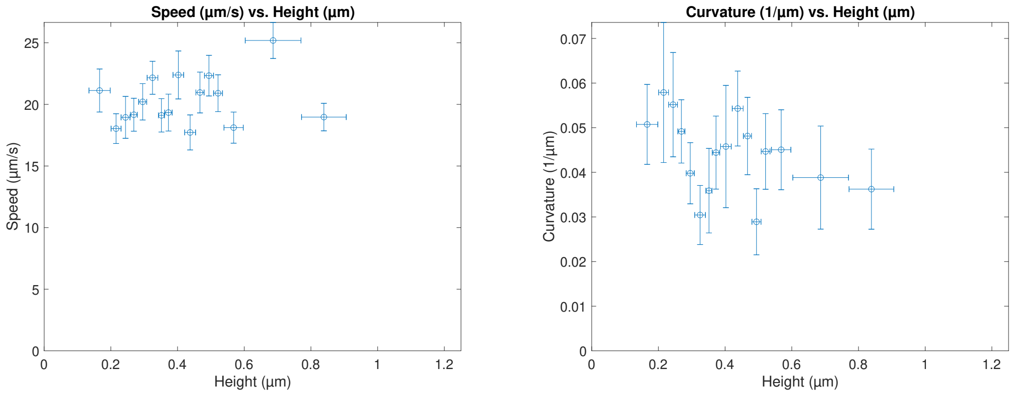

(a) (b)

Figure 3-6: Preliminary measurements of (a) cell speed as a function of height and (b) trajectory curvature as a function of height, for CheY *E. coli* swimming near a glass surface.

We also obtained preliminary measurements of θ, the angle defining the bacterium's orientation relative to the surface normal (Figure 3-3). The histogram in Figure 3-7 shows the distribution of θ values for bacteria engaged in near-surface swimming. The results suggest that bacteria were typically tilted down towards the surface while engaged in near-surface swimming. These results are consistent with hydrodynamic models, which predict that bacteria will tend to swim into the surface while engaged in near-surface swimming [1, 10]. These hydrodynamic models predict that bacteria will tend to settle into an "equilibrium angle" of about 120° from the surface normal [10]. Our experimental measurements indicate that bacteria were most frequently oriented at an angle $\theta = 100°$ relative to the surface normal, which is slightly smaller than the predicted equilibrium angle of $\theta = 120°$.

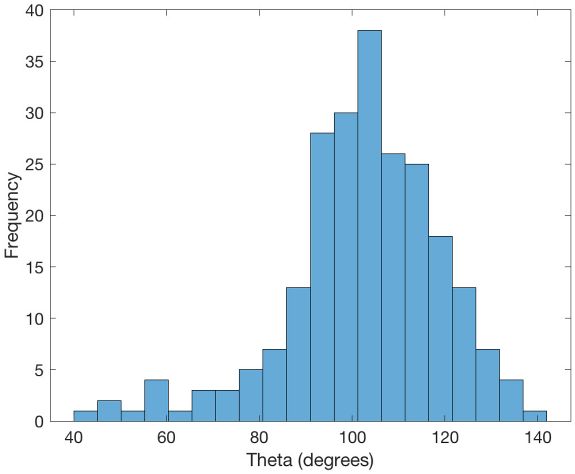

Figure 3-7: Histogram of θ values for CheY *E. coli* swimming near a glass surface.

3.9 Results: Ellipsoid-Fitting Algorithm

For most cases, the ellipsoid-fitting algorithm appears to produce a good fit when modeling bacteria. However, it should be noted that there were a few cases in which the algorithm had difficulties properly fitting the ellipsoidal model.

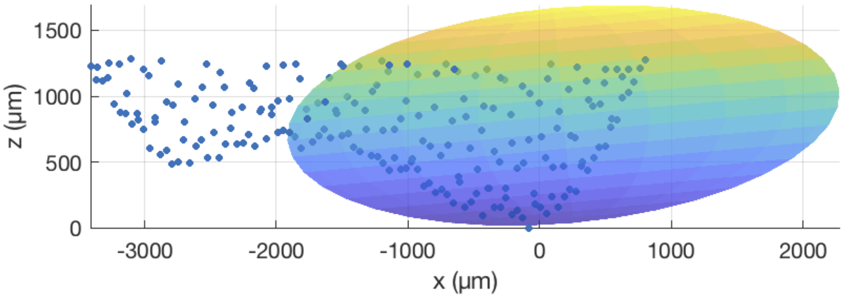

Figure 3-8: An example of a poorly-fit ellipsoidal model plotted with the original image data (blue dots). Here, the original intensity profile features two bright regions. The code has difficulty interpreting these two bright regions, and attempts to fit the ellipsoid to one of the bright regions.

In these cases, the bacterium happens to be tilted in such a way that its intensity profile contained two separate bright regions, rather than a single bright region that tapered off smoothly along the cell body.

The ellipsoid-fitting algorithm has difficulty interpreting the dip in intensity, and may attempt to fit an ellipsoid to one bright region or the other (Figure 3-8). The resulting model usually appears to have the wrong vertical orientation θ. These cases are rare enough that excluding them from analysis is unlikely to drastically affect the sample size of our measurements. Nevertheless, in the future, we plan to revise the code in order to account for these cases.

Chapter 4

Biomimetic Surfaces

4.1 Biological Environments and Near-Surface Motility

The previous chapters outline experimental and analytical protocols for measuring bacterial motility near surfaces. The goal is to optimize these protocols by reproducing published measurements for *E. coli* swimming dynamics near a glass coverslip. These protocols can then be employed in further experiments, whose purpose will be to study bacterial motility near a variety of surfaces.

Bacteria encounter a variety of complex biological environments when colonizing a host organism. A number of bacteria, including nonpathogenic *E. coli*, may populate the human gut, residing near the mucous membranes lining the intestinal epithelial tissue [15]. Here, the mucus layer produced by the mucous membranes serves an important protective role against infection, forming a viscous, charged interface with with the bacteria will interact as they navigate their surroundings. Notably, near-surface swimming above this layer has been observed in pathogenic species such as *Salmonella typhimurium* found in the gut; it is suggested that near-surface swimming may play a role in helping these bacteria "scan" the intestinal lining for topological features that can serve as targets for infection [11, 16].

Previous studies have investigated the role of certain environmental properties, such as surface geometry [17, 18] and fluid flow [19, 20], on features of near-surface swimming. For instance, near convex surfaces of sufficiently high curvature, bacteria do not remain trapped near the surface for as long a period of time [17]. Similarly, fluid flow near a surface has been shown to shorten the duration of near-surface trapping [19, 20]. These results raise the question of how other surface properties might affect near-surface dynamics.

We are interested in investigating properties such as surface viscosity, which may play a biologically relevant role for species like *E. coli* that commonly interact with viscous surfaces. In this chapter, we discuss our progress in constructing biomimetic surfaces with tunable viscosity. We outline methods for characterizing these surfaces and measuring their viscosity using the theory of Brownian motion. Our goal is to use these surfaces in bacterial motility experiments to quantify the relationship between surface viscosity and near-surface dynamics.

4.2 Biomimetic Surfaces

We are designing biomimetic surfaces of tunable viscosity for use in bacterial motility experiments. The surfaces consist of a supported lipid bilayer conjugated to 0.5 µm diameter polystyrene microspheres through biotin-avidin binding. The resulting surface is a two-dimensional colloid whose viscosity depends on the density of microspheres atop the bilayer. See Appendix A for protocols for synthesizing these surfaces. The following sections discuss methods for characterizing our biomimetic surfaces for use in bacterial motility experiments.

4.3 Characterizing the Biomimetic Surfaces

Before these surfaces can be used in bacterial motility experiments, it is important to have a good quantitative measure of how viscosity varies with microsphere density. This in turn requires a reliable method of measuring surface viscosity. We plan to measure surface viscosity by observing the diffusion of microspheres along the supported lipid bilayer. Our methodology is described in the section below.

4.3.1 Background: Brownian Motion

To understand how one can measure viscosity by observing microsphere diffusion, it is necessary to examine the situation in the context of Brownian Motion. Brownian motion refers to the random walks exhibited by particles suspended in fluid. This random walk arises from collisions between the suspended particles and the molecules comprising the fluid. It is possible to relate the motion of these particles to the properties of the particles and the surrounding fluid by constructing an equation of motion that incorporates events at both the microscopic and macroscopic level.

At the macroscopic level, the microspheres experience fluid drag. The drag force F_{drag} on the microspheres is given by Stokes' law, which considers a spherical particle with a low Reynolds number moving through a viscous fluid:

$$\vec{F}_{drag} = -6\pi\eta r\vec{u} \tag{4.1}$$

Here, η is the viscosity of the fluid, $\vec{u}$ is the velocity of the particle, and r is the radius of the particle. The acceleration of a microsphere experiencing fluid drag can then be expressed as

$$\ddot{x} = -\gamma\dot{x} \tag{4.2}$$

where $\ddot{x}$ is the acceleration of the microsphere due to fluid drag, $\dot{x}$ is the velocity of the microsphere, and γ is the constant given below:

$$\gamma = \frac{6\pi\eta r}{m} \tag{4.3}$$

Here, m represents the mass of the particle.

Simultaneously, at the microscopic level, the microspheres experience random thermal kicks. Although these kicks occur randomly, it is possible to predict their average affect on motion. On average, we expect to reproduce the following mean square velocity from equipartition of energy:

$$\langle \dot{x}^2 \rangle = \frac{kT}{m} \tag{4.4}$$

where k is the Boltzman constant, T is the temperature, and m is the mass of the particle.

At this point, we have two equations that separately describe how fluid drag and thermal kicks influence the microsphere's random walk. We can consolidate these two equations into one equation of motion, which will allow us to predict the average motion of the microspheres given certain experimental conditions. To set up the equation of motion, we begin by taking the derivative of the quantity $x\dot{x}$:

$$\frac{d}{dt}(x\dot{x}) = \dot{x}^2 + x\ddot{x} \tag{4.5}$$

where x, $\dot{x}$, and $\ddot{x}$ represent the microsphere's displacement, speed, and acceleration, respectively. We then take the average of the expression:

$$\frac{d}{dt}\langle x\dot{x} \rangle = \langle \dot{x}^2 \rangle + \langle x\ddot{x} \rangle \tag{4.6}$$

This accounts for the fact that by invoking equipartition theory in equation 4.4, the equation of motion can ultimately only consider the average motion of many particles. Substituting equations 4.2 and 4.4 into equation 4.6, we obtain

$$\frac{d}{dt}\langle x\dot{x} \rangle = \frac{kT}{m} - \gamma \langle x\dot{x} \rangle \tag{4.7}$$

The solution of the above differential equation is

$$\langle x\dot{x} \rangle = \frac{kT}{m\gamma} \tag{4.8}$$

which can be integrated to yield the following expression

$$\langle x^2 \rangle = 2 \cdot \frac{kT}{m\gamma} t \tag{4.9}$$

where $\langle x^2 \rangle$ is the mean squared displacement of the microspheres at some time t. Finally, converting γ back to the expression in equation 4.3, we obtain the expression

$$\langle x^2 \rangle = \frac{kT}{3\pi\eta r} t \tag{4.10}$$

which shows $\langle x^2 \rangle$ to be mass-independent.

The microspheres in our biomimetic surfaces are 0.5 µm in diameter, leaving them in a size regime where they will undergo Brownian motion that can be tracked with fluorescence microscopy. According to equation 4.10, the mean squared displacement of the microspheres will be related to properties of the experimental setup, such as microsphere size, temperature, and viscosity of the surrounding medium. Therefore, by observing the motion of the microspheres over time, it is possible to measure the viscosity of the medium, given the microspheres' size and the temperature of the medium.

4.3.2 Methods: Extracting Viscosity Measurements

In this section, we describe the experimental and computational methods used to extract viscosity measurements. Experiments begin by adding fluorescent microspheres to the sample of interest. We record the motion of the microspheres over time using epifluorescence microscopy. The microscopy data is then passed to custom MATLAB code that tracks the microspheres and records their displacement at each timestep. The code then goes through a series of steps to extract measurements of the viscosity of the surrounding fluid.

First, the code plots the distribution of microsphere displacements at a particular time t. The displacement x of a given microsphere is a random variable, so the displacement measurements are normally distributed. This allows us to approximate the microsphere displacements as a time-dependent Gaussian. We apply a Gaussian fit to the data, which takes the form of

$$f(x) = \frac{1}{\sigma\sqrt{2\pi}} e^{-\frac{1}{2}(\frac{x-\mu}{\sigma})^2} \tag{4.11}$$

where x is microsphere displacement, μ is the mean displacement, and σ is the standard deviation, also known as the square root of the variance. The variance of the random variable x is equal to the mean squared error in x:

$$\sigma^2 = \langle (x-\mu)^2 \rangle \tag{4.12}$$

Because their motion is random, microspheres are equally likely to be displaced in any one direction; therefore, the expected mean displacement μ is 0. Equation 4.12 then simplifies to

$$\sigma^2 = \langle x^2 \rangle \tag{4.13}$$

Note that $\langle x^2 \rangle$ appeared earlier in equation 4.10. Combining equations 4.10 and 4.13, we obtain

$$\sigma^2 = \langle x^2 \rangle = \frac{kT}{3\pi\eta r} t \tag{4.14}$$

which suggests that the variance in the microsphere displacements is time-dependent. Specifically, variance is linearly proportional to time. In the context of the experiment, this reflects the fact that as time goes on, some of the microspheres have spread farther out from their original positions.

Starting at t=0, we fit a Gaussian to the microsphere displacement data for increasing values of t (see Figure 4-1). We then record the variance of the Gaussian fit for each time t. The variance, or mean squared displacement of the microspheres, can then be plotted as a function of time t (see Figure 4-2). We then apply a linear regression to the data. By equation 4.14, the slope of the linear fit is given by

$$M = \frac{kT}{3\pi\eta r} \tag{4.15}$$

where M is the slope. This expression consists mainly of quantities that are known, such as the temperature T, the Boltzman constant k, and microsphere radius r, or things we can measure, such as m. The only remaining unknown is η, the viscosity of the fluid. Rearranging for η, equation 4.15 becomes

$$\eta = \frac{kT}{3\pi M r} \tag{4.16}$$

allowing us to easily calculate η.

4.3.3 Experiment: Validating the Methodology

As an initial validation step, we attempted to reproduce the known viscosity of water by observing the Brownian motion of freely diffusing microspheres. We suspended fluorescent polystyrene microspheres in deionized water and recorded their motion using epifluorescence microscopy. We used 1.0 µm streptavidin-coated microspheres similar to those used to construct the biomimetic surfaces. The microscopy data was then passed to our custom MATLAB code to extract viscosity measurements as described in Section 4.3.2. Preliminary results are summarized in Figures 4-1 and 4-2.

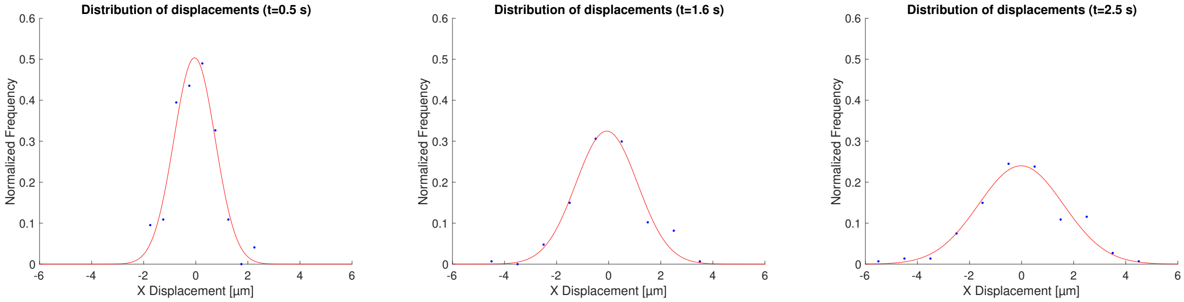

(a) (b) (c)

Figure 4-1: Distribution of the microspheres' x-displacements after (a) 0.5, (b) 1.6, and (c) 2.5 seconds. A Gaussian fit (red line) was applied to the experimental data (blue dots). As time increases, a greater fraction of the microspheres have diffused away from their initial positions, yielding a wider distribution.

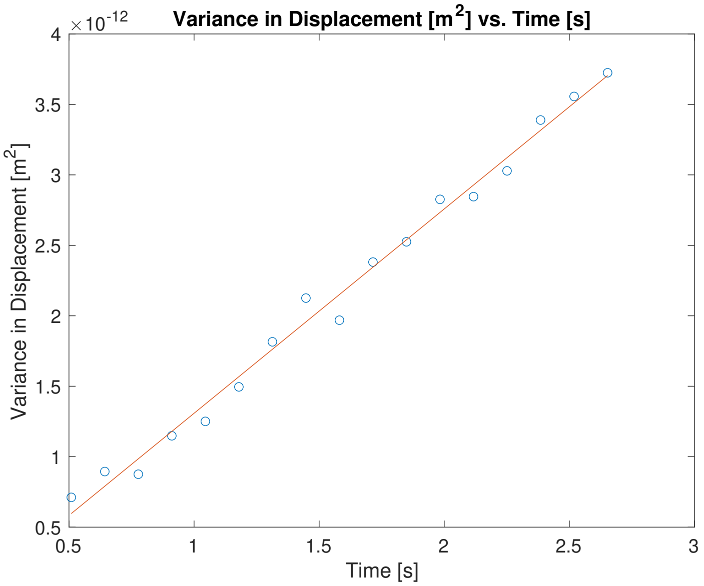

Figure 4-2: Mean squared displacement of 1.0 µm-diameter microspheres suspended in deionized water plotted as a function of time.

The measured viscosity of water, $(1.18 \pm 0.02) \times 10^{-3} Pa \cdot s$, was larger than the accepted value, $1.10 \times 10^{-3} Pa \cdot s$. One potential source of error may arise from the fact that the microspheres were recorded while diffusing less than about 1.0 µm above the coverslip. It is possible that boundary effects near the coverslip affected the motion of the microspheres, increasing the measured viscosity value. To determine the extent to which boundary effects could influence our viscosity measurements, MATLAB code was written to calculate the drag force on a sphere translating parallel to a boundary as a function of the sphere's distance from the boundary [21]. The results are plotted in Figure 4-3. Within at least 5 µm above the boundary, the drag force on a sphere appears to increase noticeably compared to the drag force away from the boundary.

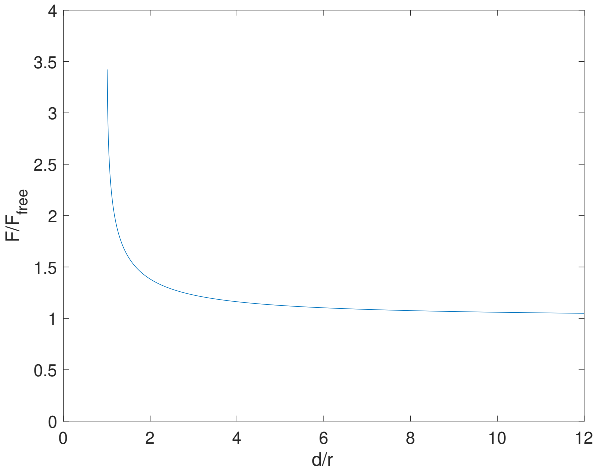

Figure 4-3: Scaled fluid drag force on a sphere translating parallel to a boundary as a function of scaled sphere-boundary separation distance. The scaled sphere-boundary separation distance, d/r, is the ratio between the actual sphere-boundary separation distance d and the radius r of the sphere. The scaled fluid drag force is the ratio between F and F_{free}, where F is the surface-parallel component of the drag force on a sphere at a height d/r above the boundary, and F_{free} is the surface-parallel component of the drag force on a sphere free from boundary effects.

4.3.4 Next Steps

Before we use this method to measure the viscosity of biomimetic surfaces, it is important to address any potential boundary effects. Because the microspheres will be tethered to the supported lipid bilayer, they will be diffusing very close to a boundary, which could potentially affect viscosity measurements. To address this issue, we plan to establish a quantitative measure of how the measured viscosity depends on height above the surface. The initial validation experiment will be repeated, this time varying the z-position of the plane of focus. Once again, fluorescent microspheres will be suspended in deionized water above a glass coverslip. First, the microscope will be focused at the glass surface ($z = 0 \mu m$), and microsphere motion will be recorded. The plane of focus will then be raised to 0.5 µm above the surface, and microsphere motion will be recorded. The process will be repeated up to 5 µm above the surface. The data could then be used to quantify the relationship between measured viscosity and height. We would expect microspheres diffusing further from the surface to yield a viscosity value closer to the accepted value for water.

Once we are able to reliably measure surface viscosity, we will run experiments to determine how surface viscosity varies with microsphere density. We will prepare surfaces with varying microsphere densities, measure the viscosity of each surface, and analyze the results to obtain a quantitative relationship between surface viscosity and microsphere density. It will then be possible to tune surfaces to a desired viscosity by adding the proper amount of microspheres to the bilayer.

4.4 Issues with biomimetic surface synthesis

Here we discuss current progress on constructing and characterizing the biomimetic surfaces. Briefly, our initial strategy for synthesizing the biomimetic surfaces was as follows. First, we used vesicle rupture to form a supported lipid bilayer (SLB) on a microscope coverslip. The SLB consists of three types of lipids: DOPC, DiI, and DOPE-biotin. DOPC comprises the majority of the bilayer. DiI contains a red fluorescent dye that allows for visualization of the bilayer. DOPE-biotin is a lipid conjugated to a biotin protein. When DOPE-biotin is incorporated into the SLB, the biotin protrudes from the bilayer. These biotin proteins can bind strongly to another protein called avidin. We took advantage of the strong biotin-avidin binding affinity to tether microspheres to the SLB. Specifically, we deposited streptavidin-coated microspheres onto the SLB and allowed them to bind to biotin proteins belonging to DOPE-biotin in the membrane. Once these microspheres became bound to DOPE-biotin, they should then have been able to diffuse along the surface of the bilayer.

A few issues in the synthesis needed to be addressed. First, producing a good SLB by vesicle rupture proved to present certain challenges. The SLBs we produced seemed to exhibit a number of strange topological features that appeared to be clumps of lipids; washing the bilayer proved ineffective in removing these features. The streptavidin-coated beads would stick to these features, which covered most of the SLB, and fail to diffuse properly. To determine whether the bilayer itself was intact, we performed FRAP experiments on the SLB. We found that the bilayer itself did show recovery after photobleaching, suggesting

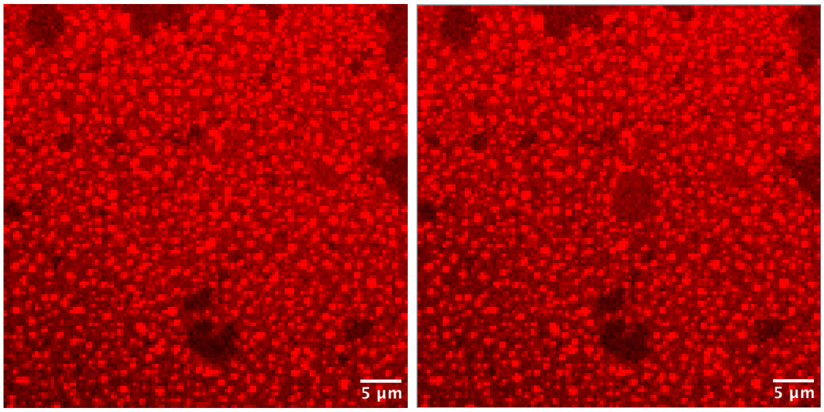

(a) (b)

Figure 4-4: A supported lipid bilayer (SLB) consisting of DOPC, DiI, and DOPE-biotin, shown (a) before, and (b) after photobleaching. Bright red blotches are suspected to be clumps of lipids settled on top of the SLB, which is suspected to be the dimmer red background. It appears that the only the SLB underneath the clumped lipids shows recovery after photobleaching.

that the SLB was forming properly. When we photobleached a region containing the strange topological features, those features did not show recovery after photobleaching. We suspect that these features came from unruptured vesicles that had somehow become clumped atop the bilayer. As a result, avidin-coated beads would stick to debris on the bilayer and become immobilized, rather than tethering properly to a biotinylated lipid and freely diffusing.

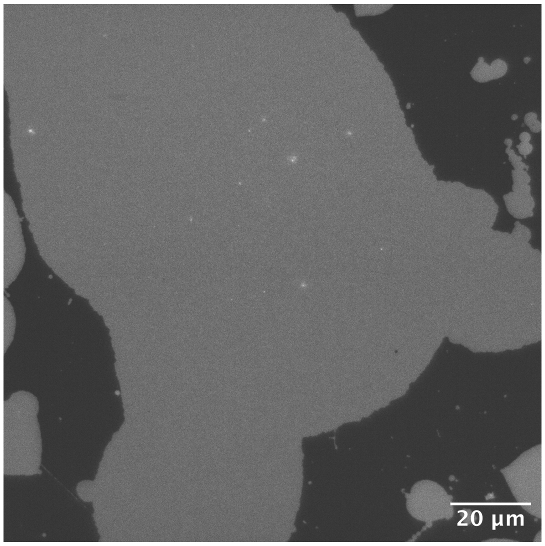

Figure 4-5: Patches of supported lipid bilayer (light grey regions) created by GUV rupture.

To avoid this issue, we switched to rupturing GUVs (Giant Unilamellar Vesicles) to create patches of bilayer, rather than rupturing SUVs to create one continuous bilayer. Using this method, we were able to successfully make patches of bilayer on a glass coverslip 4-5. These bilayer patches did not exhibit any clumped lipid patches, and excess vesicles on the surface could be removed with PBS washes with relative ease. That being said, there are drawbacks to using the bilayer patches produced by GUV rupture instead of the SLB. The advantage of the SLB is that there is continuous biomimetic surface throughout the field of view. By contrast, the bilayer patches only allow us to synthesize localized regions of biomimetic surfaces, which limits the data we can collect in a given field of view. Furthermore, the streptavidin-coated beads still did not bind properly to the bilayer. All microspheres, whether they became stuck to the glass coverslip or to the bilayer patches, became immobile once they bound to the surface.

One possible explanation for why the microspheres showed no movement along the bilayer is that the microspheres were diffusing over such a long timescale that they appeared immotile. To investigate this possibility, we calculated the time it should take for the microspheres to move a distance equal to their own diameter. Rearranging equation 4.10, the relationship between time and mean squared displacement can be written as

$$t = \frac{3\pi\eta r}{kT}\langle x^2\rangle \tag{4.17}$$

where η is viscosity and r is the radius of the microsphere. For a 1.0 µm-diameter microsphere diffusing in water of viscosity $\eta = 1.0 \times 10^{-3} Pa \cdot s$ at room temperature ($T = 293K$), the time it would take the microspheres to reach a mean squared displacement of one diameter is about 1.2 seconds. Therefore, it is unlikely that the microspheres are diffusing too slowly to be observed experimentally. Another plausible explanation is that some aspect of the preparation process is causing the streptavidin coating the microspheres to denature. The denatured streptavidin proteins would be unable to bind properly to biotinylated lipids in the bilayer. Future work will investigate ways to ensure that the microspheres properly diffuse along the bilayer.

Chapter 5

Conclusion

In this thesis, we devised new experimental and computational methods to study the dynamics of bacteria swimming near surfaces. We used TIRF microscopy to record near-surface swimming, then passed the microscopy data through custom MATLAB code to extract measurements of swimming speed, trajectory curvature, and cell height above the surface. The MATLAB code tracks the bacteria, reconstructs their trajectories in three dimensions by modeling the bacteria as ellipsoids, then extracts dynamical measurements. Our ellipsoidal modeling code, in most cases, successfully reconstructs the bacterium's position in space. However, the ellipsoid-fitting code does fail to model a few specific cases, which will be addressed in future work. We used our code to take preliminary measurements of bacterial swimming dynamics above a glass coverslip. Future work will aim for a quantitative match with published literature in order to validate our methodology.

Once we have validated our methods, we plan to study swimming dynamics near biomimetic surfaces, which we will use to study the effect of specific surface properties on near-surface swimming. We have begun to develop viscous biomimetics surfaces and devised methods to characterize the surfaces. We have prepared the individual parts of the biomimetic surfaces, including small polystyrene microspheres and a lipid bilayer supported on a glass coverslip. However, although the microspheres appear to be binding to the lipid bilayer, we have not yet observed the microspheres freely diffusing along the surface. Being able to record this diffusion will be critical for measuring the viscosity of the surface, which can be extracted by observing the Brownian motion of the microspheres. As an initial validation step, we observed the Brownian motion of microspheres suspended in water, and attempted to reproduce the known viscosity of water. We obtained a value slightly larger than would be expected within error, which could be explained by boundary effects near the surface; near a surface, the drag force on the microspheres is larger, which could cause us to measure a larger viscosity value than would be expected in bulk fluid. Future work will aim to properly synthesize the biomimetic surfaces, then validate our methods for measuring their viscosity. Ultimately, we aim to study the effect of a number of surface properties, including viscosity and charge, on near-surface dynamics. Such studies will inform future research into near-surface swimming.

Chapter 6

Appendix A

6.1 Procedure: Cleaning Glass-Bottom Dishes

Samples were placed in 35-mm diameter glass round-bottom dishes during observation. Dishes were cleaned thoroughly before use. First, the dishes were sonicated in (1) 3 M KOH, (2) ethanol, and (3) deionized water for 30 minutes each, rinsing dishes 5 times with deionized water after each round of sonication. The sonicated dishes were dried with nitrogen. Finally, the dried dishes were plasma cleaned for 12 minutes at 0.8-0.9 torr, cycling the RF level three times as follows: 3 minutes on medium, 1 minutes off.

6.2 Procedure: Preparing Microsphere Solutions

The microspheres used in these experiments were streptavidin-coated green fluorescent polystyrene microspheres with a diameter of 0.5 µm. Microspheres were obtained from BangsLabs in a stock solution of 1.1% solids. We prepared the microspheres for use in our experiments as follows. First, 0.5 µL of microsphere stock was added to 1000 µL of distilled water in an eppendorf tube. The solution was vortexed for 20 seconds to mix the beads into solution. Next, two preliminary washes were done to remove additives such as EDTA, anti-microbial, and surfactant that were originally in the microsphere stock solution. Washes were performed as follows: (1) The microsphere solution was centrifuged at 11000 rcf for 5 minutes, (2) 750 µL of supernatant was carefully removed, (3) 750 µL of distilled water was added, and (4) the solution was vortexed for 20 seconds to resuspend the microspheres.

6.3 Procedure: Synthesizing Biomimetic Surfaces

The supported lipid bilayers consist of three types of lipids: DOPC, or 1,2-bioleoyl-sn-glycero-3-phosphocholine, which comprises the majority of the bilayer; DOPE-biotin, or 1,2-Dioleoyl-sn-Glycero-3-Phosphoethanolamine-N-(Cap Biotinyl)(Sodium Salt), which serves to tether avidin-coated microspheres to the bilayer; and DiI, or 1,1'-Dioctadecyl-3,3,3',3'-Tetramethylindocarbocyanine Perchlorate, a red dyed lipid that allows for visualization of the bilayer. Lipids were obtained from Avanti Lipids, dissolved in chloroform. The following sections describe the two different methods used to form supported lipid bilayers for our biomimetic surfaces.

6.3.1 Method 1: Small Unilamellar Vesicle Rupture

The lipids were added to a test tube in the desired quantities to make a solution of 98.8% DOPC, 1.0% DiI, and 0.2% DOPE-biotin. The lipids were dried with nitrogen, then vacuumed for 1 hour to remove residual chloroform. The dried lipids were rehydrated with 250 µL of distilled water. Next, small unilamellar vesicles (SUVs) were formed by extrusion. The rehydrated lipid solution was passed through a filter with a pore size of 0.4 µm 21 times, then passed through a filter with a pore size of 0.03 µm one time, ultimately producing SUVs with a diameter of 0.03 µm. The volume of the final SUV solution was doubled with warm 1X PBS.

Next, the SLB was formed by vesicle rupture. 1000 µL of salt solution (100 mM $CaCl_2$) was pipetted onto a clean glass bottom dish. Immediately afterwards, 200 µL of the SUV solution was added to the $CaCl_2$. The solution was incubated at 37°C for 30 minutes to encourage rupture. Following incubation, the SLB was rinsed at least 12 times with 150 µL of distilled water. Any excess solution outside of the central well was drawn off, being careful not to deplete volume from the central well and expose the bilayer. Microspheres (see Section 6.2) were deposited onto the SLB and allowed to bind to DOPE-biotin in the bilayer.

6.3.2 Method 2: Giant Unilamellar Vesicle Rupture

Lipids were added to a test tube in the desired quantities to make a solution of 98.8% DOPC, 1.0% DiI, and 0.2% DOPE-biotin. The lipid mixture was used to form a thin film of lipids on the conducting side of two indium tin oxide-coated glass slides (Sigma Aldrich #7031928 − 12Ω/sq) glass slides. Specifically, 5 µL of lipid solution was dispensed along one edge of the slide using a Hamilton syringe; immediately afterwards, the edge of the pipette tip was drawn across the slide to spread the droplet of lipid solution, forming a thin film. The slides were vacuumed for 1 hour to remove residual chloroform.

Next, giant unilamellar vesicles (GUVs) were formed by electroformation. To assemble the electroformation chamber, a small gasket was placed between the two slides, with the conducting side of the slides facing inwards. The gasket was cut to leave a small opening at the top. Two strips of copper tape were obtained; a piece of copper tape was placed between the gasket and each of the slides to serve as electrical leads. The apparatus was held together with binder clips. The end result is a small chamber in which GUVs may be formed.

To begin forming GUVs, the electroformation chamber was filled with a 250 mM sucrose solution. The chamber opening was sealed with modeling clay, and the copper leads were connected to a function generator. The solution was incubated at 55 − 60 °C while an electric current was run through the leads. The current was adjusted as follows. First, we applied an 80 mV sine wave with a frequency of 10 Hz for 3 minutes. We then applied a 100 mV sine wave with the same frequency for 3 minutes. From there, the voltage was raised by 50 mV every 3 minutes, keeping the frequency constant at 10 Hz. Once the voltage reached 500 mV, we maintained the 500 mV sine wave at a frequency of 10 Hz for 2 hours. Finally, a 1.2 V square wave with a frequency of 5 Hz was applied for 30 minutes. Afterwards, the current was switched off and the chamber was allowed to cool to room temperature for at least 1 hour. GUVs were gently transferred to an eppendorf tube, and the volume was doubled with 250 mM sucrose solution. GUVs were typically used within one day of preparation.

Patches of supported lipid bilayer were then formed by vesicle rupture. About 300 µL of 250 mM sucrose solution and 50 µL of 1X PBS were pipetted into a clean glass-bottom dish, followed by 50 µL of the GUV solution. GUVs were allowed to rupture for about 30 minutes. The resulting patches of bilayer were rinsed at least 12 times with 1X PBS to remove unruptured vesicles. Before adding microspheres to the bilayer, the solution was exchanged for deionized water through at least 12 deionized water rinses; this prevents the microspheres from immediately aggregating. Microspheres were deposited onto the bilayer patches and allowed to bind to DOPE-biotin in the bilayer.

Bibliography

[1] Eric Lauga et al. “Swimming in Circles: Motion of Bacteria near Solid Boundaries”. In: *Biophysical Journal* 90.2 (2006), pp. 400–412. DOI: 10.1529/biophysj.105.069401.

[2] Knut Drescher et al. “Fluid dynamics and noise in bacterial cell-cell and cell-surface scattering”. In: *Proceedings of the National Academy of Sciences* 108.27 (2011), pp. 10940–10945. DOI: 10.1073/pnas.1019079108.

[3] Davide Giacché, Takuji Ishikawa, and Takami Yamaguchi. “Hydrodynamic entrapment of bacteria swimming near a solid surface”. In: *Physical review. E* 82.5 Pt 2 (2010), p. 056309. DOI: 10.1103/PhysRevE.82.056309.

[4] Diego Lopez and Eric Lauga. “Dynamics of swimming bacteria at complex interfaces”. In: *Physics of Fluids* 26.7 (2014), p. 071902. DOI: 10.1063/1.4887255.

[5] Guanglai Li, Lick-Kong Tam, and Jay X. Tang. “Amplified effect of Brownian motion in bacterial near-surface swimming”. In: *Proceedings of the National Academy of Sciences* 105.47 (2008), pp. 18355–18359. DOI: 10.1073/pnas.0807305105.

[6] Paul D. Frymier et al. “Three-dimensional tracking of motile bacteria near a solid planar surface”. In: *Proceedings of the National Academy of Sciences* 92.13 (1995), pp. 6195–6199. DOI: 10.1073/pnas.92.13.6195.

[7] Paul D. Frymier and Roseanne M. Ford. “Analysis of bacterial swimming speed approaching a solid–liquid interface”. In: *AIChE J.* 43.5 (1997), pp. 1341–1347.

[8] Eric Lauga. “Bacterial Hydrodynamics”. In: *Annual Review of Fluid Mechanics* 48.1 (2016), pp. 105–130. DOI: 10.1146/annurev-fluid-122414-034606.

[9] Emiliano Perez Ipiña et al. “Bacteria display optimal transport near surfaces”. In: *Nat. Phys.* 15 (2019), pp. 610–615. DOI: 10.1038/s41567-019-0460-5.

[10] Margot A.-S. Vigeant et al. “Reversible and irreversible adhesion of motile Escherichia coli cells analyzed by total internal reflection aqueous fluorescence microscopy”. In: *Applied and Environmental Microbiology* 68.6 (2002), pp. 2794–2801.

[11] Benjamin Misselwitz, Naomi Barrett, and Saskia et. al. Kreibich. “Near surface swimming of Salmonella Typhimurium explains target-site selection and cooperative invasion”. In: *PLoS pathogens* 8 (7 2012), e1002810. DOI: 10.1371/journal.ppat.1002810.

[12] T.S.J. Elliot et al. “Novel approach to investigate a source of microbial contamination of central venous catheters”. In: *European journal of clinical microbiology & infectious diseases* 16 (3 1997), pp. 37–44. DOI: 10.1007/BF01709583.

[13] Garth A. James et al. “Biofilms in chronic wounds”. In: *Wound repair and regeneration* 16 (1 2008), pp. 37–44. DOI: 10.1111/j.1524-475X.2007.00321.x.

[14] Kenneth N. Fish. “Total internal reflection fluorescence (TIRF) microscopy”. In: *Current protocols in cytometry* 50 (2009), pp. 12.18.1–12.18.13. DOI: 10.1002/0471142956.cy1218s50.

[15] Tyrell Conway and Paul S. Cohen. “Commensal and Pathogenic Escherichia coli Metabolism in the Gut”. In: *Microbiology spectrum* 3 (3 2015). DOI: 10.1128/microbiolspec.MBP-0006-2014.

[16] Markus Furter et al. “Mucus Architecture and Near-Surface Swimming Affect Distinct Salmonella Typhimurium Infection Patterns along the Murine Intestinal Tract”. In: *Cell Reports* 27.9 (2019), 2665–2678.e3. DOI: https://doi.org/10.1016/j.celrep.2019.04.106.

[17] O. Sipos et al. “Hydrodynamic Trapping of Swimming Bacteria by Convex Walls”. In: *Physical Review Letters* 114 (24 2015), p. 258104. DOI: 10.1103/PhysRevLett.114.258104.

[18] I.D. Vladescu et al. “Filling an emulsion drop with motile bacteria”. In: *Physical Review Letters* 113 (26 2014), p. 268101. DOI: 10.1103/PhysRevLett.113.268101.

[19] Mehdi Molaei and Jian Sheng. “Succeed escape: Flow shear promotes tumbling of Escherichia colinear a solid surface”. In: *Scientific reports* 6 (2017), p. 35290. DOI: 10.1038/srep35290.

[20] Jules D.P. Valentin et al. “Substrate viscosity plays an important role in bacterial adhesion under fluid flow”. In: *Journal of Colloid and Interface Science* 552 (2019), pp. 247–257. ISSN: 0021-9797. DOI: https://doi.org/10.1016/j.jcis.2019.05.043.

[21] M. E. O’Neill. “A Slow motion of viscous liquid caused by a slowly moving solid sphere”. In: *Mathematika* 11.1 (1964), pp. 67–74. DOI: 10.1112/S0025579300003508.